Facile synthesis of Ag nanoparticles-decorated WO_3 nanorods and their application in O_2 sensing

Yiyun Zhu [a], Chris Blackman [a,*], Pengfei Zhou [a,c,d], Sai Kiran Ayyala [b], James A. Covington [b], Yanbai Shen [d], Jinsheng Liang [c], Xiangxi Zhong [b,c], Caroline Knapp [a], Ye Zhou [a]

[a] Department of Chemistry, University College London, London WC1H 0AJ, United Kingdom
[b] School of Engineering, University of Warwick, Coventry CV4 7AL, United Kingdom
[c] Key Laboratory of Special Functional Materials for Ecological Environment and Information, Hebei University of Technology, Ministry of Education, Tianjin 300130, China
[d] School of Resources and Civil Engineering, Northeastern University, Shenyang 110819, China

ARTICLE INFO

ABSTRACT

Here we describe a two-step aerosol-assisted chemical vapor deposition (AACVD) synthesis method for the fabrication of Ag nanoparticles (NPs) decorated WO_3 nanorods (NRs), evaluating the use of different organometallic silver precursors. Physical property characterization techniques including XRD, SEM, TEM, and XPS were carried out to investigate the composition and morphology of the pristine WO_3 NRs and functionalized WO_3 NRs with Ag NPs. The results showed that uniform WO_3 NRs were obtained with a length of 600 nm to several μm and a diameter of 100–200 nm, and Ag NPs were well-dispersed on the surface of WO_3 NRs with the size of 6–20 nm. The nanostructured WO_3 thin films were synthesized and integrated directly onto alumina platforms via the AACVD method to fabricate gas sensors. Gas sensing performance was investigated towards different O_2 concentrations between 1% and 20% at various operating temperatures. The sensing response revealed that an increase in baseline resistance was observed for the Ag-decorated WO_3 sensors fabricated by using organometallic silver precursors, and the decoration of Ag NPs on WO_3 sensors improved sensing properties as compared to the undecorated ones. The possible formation process and sensing mechanism of the Ag NPs decorated WO_3 NRs are proposed.

1. Introduction

O_2 sensors are in high demand for environmental monitoring, food security, health care, and industrial processing [1,2]. Nowadays, the widely used electrochemical-based O_2 sensors rely on the oxidation of Pb in the anode, which is highly toxic to the environment and should be replaced in the near future according to the "Restriction of Hazardous Substances Directive" (RoHS). Though Pb-free alternative electrochemical gas sensors to O_2 have been produced by introducing Zn, Fe, or Al, issues such as short lifespan and low sensitivity still remain. Meanwhile, the current alternative oxygen gas sensors still cannot meet the need for cost-effective, compact, and low-temperature working devices. Based on this, we previously deposited Ag/Ag_2O nanoparticles (NPs) on the surface of WO_3 nanorods to fabricate Pb-free gas sensors for O_2 measurement in a highly humid environment [3].

Metal-oxide semiconductor (MOS) gas sensors have been widely studied and used in gas detection fields due to the advantages of low cost, compact size, simple measurement, and easy production [4,5]. MOS nanomaterials can be divided into n-type and p-type metal oxide semiconductors based on their resistance response to gases classed as 'oxidizing' or 'reducing'. Tungsten oxide (WO_3) is an important n-type MOS with a bandgap between 2.4 and 2.8 eV that has attracted wide attention due to its unique physical and chemical properties, and it has been used in gas sensing, electrochromic, photochromic, and catalytic fields [6,7]. It has been reported as an ideal candidate for the detection of various gases including NO_2 [8], NH_3 [9], H_2S [10], H_2 [11], and O_2 [3]. Therefore, here WO_3 is explored as a potential oxygen gas-sensing material to replace Pb-bearing ones.

Over the last few decades, many fabrication methods have been developed and used to prepare WO_3 nanostructures, including chemical vapor deposition [12], hydrothermal method [13], thermal evaporation [14], template-assisted growth [15], etc. Chemical vapor deposition (CVD), as a conventional technique for the synthesis of solid-state thin films, has been applied for many years. High-purity
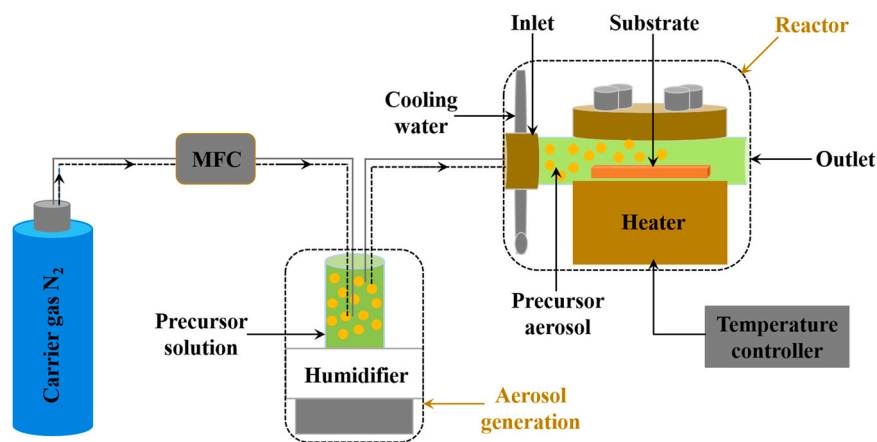
Fig. 1. Schematic diagram of the reaction process of AACVD technique.

materials with structural control at the atomic or nano-scale can be obtained by using the CVD method. However, the general lack of readily available volatile precursors and the difficulty in controlling the stoichiometry of the deposits hinder the further development of CVD technique. As an important branch of conventional CVD, aerosol-assisted chemical vapor deposition (AACVD) technique uses aerosol droplets to transport the chemical precursors onto the substrate in the reactor with the aid of an inert gas carrier (usually N_2 or Ar) [16,17]. A wide range of low volatility or thermally unstable precursors can be used at an ambient atmosphere or low temperature due to the process relying principally on the solubility of the chemical precursor instead of volatility. Nano-thin films synthesized via AACVD show excellent control in particle size, crystallinity, porosity, and stoichiometry. Besides, the morphologies of the thin films can also be controlled by simply adjusting various reaction condition parameters such as deposition operating temperature, choice of solvent, and gas flow rate in the AACVD process. AACVD is commonly applied to synthesize metal oxide nanostructures for use in gas sensors [18].

WO$_3$ nanorods (NRs) decorated with various noble metal NPs have been widely investigated and developed in many applications, especially in the gas sensing area [19,20]. Many studies have proved that the gas sensing response of a target analyte gas can be greatly enhanced by adding noble metal NPs onto the MOS sensing material and it has been demonstrated that AACVD is also a flexible technique that facilitates the implementation and functionalization of WO$_3$ NRs with many different noble metals [3,21,22]. In this paper, undecorated WO$_3$ NRs were prepared by using AACVD first and then noble metal additive, Ag, was further deposited onto the surface of the as-prepared WO$_3$ NRs. In previous work in this area, commercially available AgNO$_3$ was used to produce Ag/Ag$_2$O NPs decorating particles on nanostructured WO$_3$ [3], but that Ag-precursor was only capable of producing low loadings even at high precursor concentrations. To control Ag-loading, an alternative silver precursor is required. The organometallic silver precursors used here have previously been used to make Ag NP via a hydrothermal reaction [23] but never previously for AACVD and provide controllable deposition of Ag NP on the surface of WO$_3$ NRs. The composition and morphology of the as-deposited WO$_{3−x}$ and WO$_3$ after annealing (AA) thin films were characterized by XRD, SEM, TEM, and XPS. The diameter of the Ag NPs was measured and the particle size distribution

of the Ag NPs was counted. Finally, gas sensing performance towards oxygen for the bare WO$_3$ NRs and Ag-decorated WO$_3$ NRs were tested and the sensing mechanism of Ag-functionalized WO$_3$ towards O$_2$ is discussed.

2. Experimental

2.1. Preparation of sensing material and gas sensor

WO$_3$ NRs were synthesized using AACVD on the surface of alumina sensor platforms. The size of each platform was 2 × 2 mm with a thickness of 250 µm. Gold interdigitated electrodes were printed on one side of the platform and platinum heater on the other side. The cleaned platforms were placed close to the outlet of the rectangular AACVD reactor and preheated to 375 °C. Tungsten hexacarbonyl [W(CO)$_6$] (0.06 g, 0.17 mmol) was dissolved in a mixed solution of 10 mL acetone and 5 mL methanol. This solution was then transferred to a flask. After sonicating for 5 min, an aerosol was generated by an ultrasonic humidifier (2 MHz, Johnson Matthey Liquifog) at room temperature. A gas flow of N$_2$ (99.99%, BOC) was passed through the aerosol mist at a flow rate of 300 standard cubic centimeter per minute (sccm) to transport the aerosol droplets into the preheated reaction chamber, controlled by a mass flow controller (MFC, Brooks). Under these conditions, the precursor solution was fully transferred within 30 min. A shadow mask was used during the fabrication process, aiming to control the deposition area of the sensing materials. A set of nine alumina-based gas sensors can be arranged in the mask base at a time. Once the deposition was finished, the heater and humidifier were then switched off in sequence, and the sensors were naturally cooled down to room temperature under a flow of N$_2$. The as-deposited films on the surface of sensors were annealed in a muffle furnace for 2 h in air and heated up from room temperature to 500 °C at a rate of 10 °C/min to obtain WO$_3$ NRs. The reaction process of the AACVD technique is shown in Fig. 1. Organometallic silver metal precursors, silver 2-methyl-2-amino-propan-1-ol (Ag-AMP), silver 1-aminopropan-2-ol (Ag-AP), and silver 2-aminoethanol (Ag-EA), were synthesized according to the literature method [23] and then deposited via AACVD on the annealed WO$_3$ gas sensors at a heating temperature of 275 °C and N$_2$ flow rate of 170 sccm. Depositions with various volumes of the Ag precursor solutions were carried out to explore the effect of different
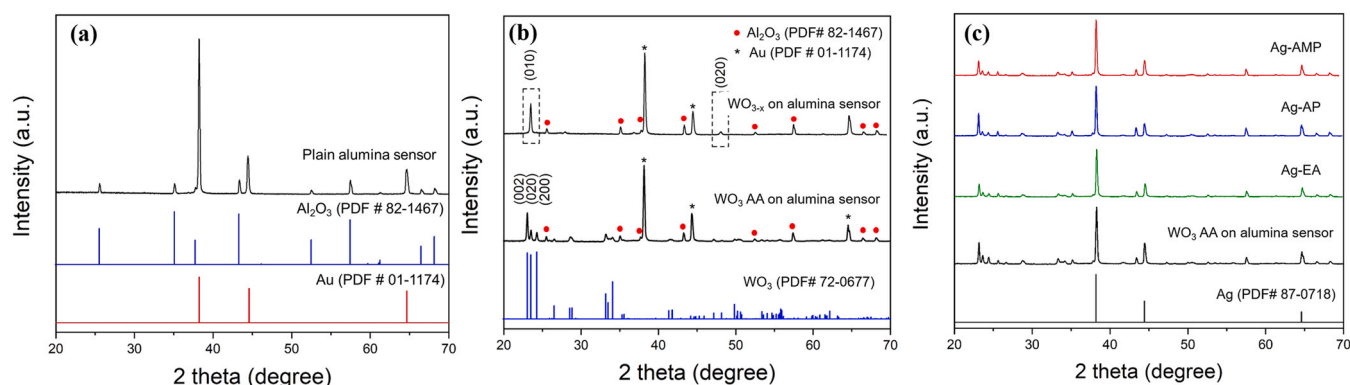
Fig. 2. XRD patterns of (a) plain alumina sensor, (b) as-deposited WO_{3-x} and WO_3 AA at 500 °C in the air for 2 h on alumina sensor platform, (c) as-deposited Ag decorated WO_3 sensors by using three organometallic Ag metal precursors.

Ag-loading on WO_3 gas sensors for gas sensing performance towards oxygen.

2.2. Structural characterization

The crystalline structures of the synthesized thin-film materials were obtained by X-Ray Diffraction (XRD) (Bruker D8-Discover) equipped with a silicon strip detector using Cu Kα radiation ($\lambda = 1.5418$ Å) and operated at a current of 40 mA and a voltage of 40 kV. The X-ray diffraction patterns were collected with a scanning rate of 0.05°/s over a 2θ scan range from 20° to 70°. A field emission scanning electron microscope (FESEM) (JEOL JSM-6301/JSM-6300) with the energy of 5/15 keV was used to identify the morphology of the thin films from a top-down configuration after Au-coating. High-resolution transmission electron microscopy (HR-TEM) measurements were performed on a JEOL 2100 at a voltage of 200 kV. X-ray photoelectron spectroscopy (XPS) (Thermo Fisher Scientific) with a monochromatic Al Kα X-Ray source (1846.6 eV) was used to measure the elemental composition and electronic states of the elements. C 1s (284.8 eV) peak calibration is conducted for the referencing of the other peaks' binding energy.

2.3. Gas sensing characterization

A predefined concentration of oxygen was obtained by diluting zero air (20% O_2) with nitrogen (99.999%) provided by the gas rig (Lehman Instrument, France). The variance in the concentration of oxygen was achieved by changing the flow rate of each gas using a mass flow controller (MFC, UFC 1100, Brooks) controlled by a computer program written in LabVIEW (National Instrument 2016). A water bubbler was added to the pathway of the tested gas mixture before entering the sensor chamber and used to simulate the humid environment. The resistance changes during the tests regarding different sensors while exposed to different concentrations of oxygen gas were monitored and recorded by a sensor management system AS-330 (Atmospheric Sensor Ltd, UK). By using this device, the sensing performance under different ranges of operating temperatures, test periods, and operating sequences can be carried out and analyzed. The time interval for the sensing test was 30 min of gas exposure. The oxygen concentration varied between 0% and 20%. The sensors were then purged with N_2 for 30 min to ensure their recovery to the baseline value of the initial resistance and stability before a new measurement was taken. The sensors' response

sensitivity was defined as being equivalent to R_g/R_a, where R_a is the resistance of sensor baseline in the nitrogen and R_g is the sensor resistance when the sensors are exposed to the target gas O_2.

3. Results and discussion

3.1. Material characterization

The XRD pattern of a plain alumina sensor platform without any deposition is shown in Fig. 2(a), which is identified as a combination of two materials obviously, corresponding to alumina and gold. Specifically, the diffraction peaks located at 25.6°, 35.2°, 37.8°, 43.4°, 52.6°, 57.5°, 66.5°, and 68.2° are respectively attributed to (012), (104), (110), (113), (024), (116), (214) and (300) reflections, which are in good agreement with the standard reference pattern of hexagonal alumina (JCPDS # 82-1467). The rest of the peaks positioned at 38.3°, 44.6°, and 64.7° can be indexed to (111), (200), and (220) planes and match well with the reference pattern of cubic gold (JCPDS # 01-1174). It is worth highlighting that alumina is the base of the sensor platform and gold comes from the electrodes. The XRD patterns of as-deposited sub-stoichiometric tungsten oxide (WO_{3-x}) and WO_{3-x} after annealing (WO_3 AA) on the alumina substrates are put together in Fig. 2(b) for comparison. Regardless of the peaks attributed by Al_2O_3 and Au, two highlighted peaks at 23.5° and 48.1° correspond to (010) and (020) reflections respectively, suggesting the formation of monoclinic phase structure of WO_{3-x} before annealing [24]. While the diffraction peaks of WO_3 AA can be indexed to monoclinic WO_3 (JCPDS # 72-0677). The strong peak at 23.1° and two relative weak peaks at 23.6° and 24.3° are ascribed to (002), (020), and (200) reflections, showing the preferred orientation along the (002) direction of WO_3 NRs deposited on the alumina substrate after annealing. Fig. 2(c) shows the XRD patterns of as-deposited Ag-decorated WO_3 gas sensors. Three organometallic Ag metal precursors with 10 μL of the initial precursor solution were deposited on the annealed WO_3 sensors at a N_2 flow rate of 170 sccm and the reaction temperature was 275 °C. No significant difference was found after the deposition of Ag-precursors on WO_3 gas sensors, the diffraction peaks of silver (38.2°, 44.3° and 64.5°, JCPDS # 87-0718) overlap with the peaks of gold (38.3°, 44.6° and 64.5°, JCPDS # 01-1174) from the electrodes contained on the surface of the gas sensor.

Fig. 3(a) shows the surface morphology of a bare sensor, which reveals that the sensor is made up of interdigitated Au electrodes and alumina-based substrate. Fig. 3(b) illustrates the cross-section of
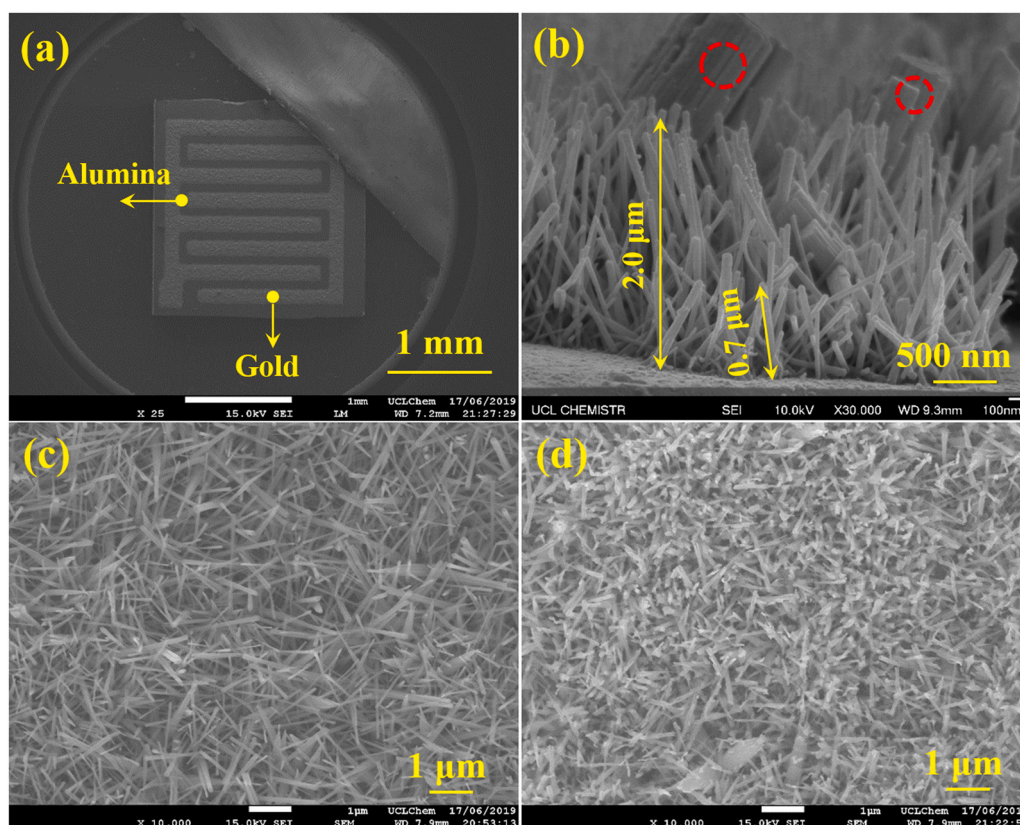
Fig. 3. SEM images of (a) bare alumina sensor, (b) cross-section of as-deposited WO$_3$ thin films on alumina platform, (c) as-deposited WO$_{3-x}$ and (d) WO$_3$ AA on alumina sensor.

as-deposited WO$_{3-x}$ thin films. A high density of randomly oriented rod-like morphology can be observed. WO$_{3-x}$ NRs show slender structure with a diameter of about 80 nm and a length ranging from 700 nm to several micrometers. It is noteworthy that some slim rods are self-assembled into bundled aggregates in the marked area, which may be ascribed to the high surface energy of the single na-norod with a high length-to-diameter ratio during the preparation process [25]. The surface morphologies of as-deposited WO$_{3-x}$ thin film before and after annealing are shown in Fig. 3(c) and 3(d). From Fig. 3(c), it can be seen that a thick layer of nonaligned WO$_{3-x}$ NRs is formed on the surface of the sensor. The distribution of WO$_3$ NRs becomes dense after annealing (Fig. 3(d)).

The microstructure of the WO$_{3-x}$ and WO$_3$ NRs was examined by HRTEM, and the corresponding results are shown in Fig. 4. In Fig. 4(a), the WO$_{3-x}$ shows a decrease in diameter from 110 nm to 20 nm, which we have previously observed [26], and with a length of 2.14 µm along the growth direction (bottom to top), which is perpendicular to the substrate. From the inset picture in Fig. 4(a), the lattice spacing of 0.362 nm can be observed, which can be attributed to the (010) plane of monoclinic WO$_{3-x}$, indicating that the growth direction of WO$_{3-x}$ NRs was along [010] direction. The sharp heads of the nanorod structure disappeared and long nanorods tend to break into short pieces after annealing at 500 °C in the air for 2 h as is shown in Fig. 4(c). Obviously, the surface of the WO$_3$ NRs became slightly coarser and rough. The lattice fringes in the inset of Fig. 4(c) revealed the D-spacing of 0.385 nm and could be ascribed to the (002) planes of monoclinic WO$_3$ (JCPDS # 72–0677), demonstrating

that the growth direction of WO$_3$ NRs was along [002] direction, which is in good agreement with the characterization analysis of XRD. Based on the two groups of interplanar spacings, it can be concluded that lattice parameters are influenced by the oxidization of WO$_{3-x}$ to WO$_3$ during the annealing process.

SEM characterizations of as-deposited Ag-decorated WO$_3$ gas sensors via organometallic Ag metal precursors, including Ag-AMP, Ag-AP, and Ag-EA with different amounts of precursor solution used for deposition, are shown in Fig. 5. It can be clearly seen that many spherical-shaped Ag NPs are uniformly decorated on the surface of WO$_3$ NRs. In particular, the coverage of the NPs on the surface of WO$_3$ NRs increases gradually as the amount of the initial precursor increases and becomes almost saturated when the dosage reaches 10 µL. No obvious morphology change for Ag NPs is found with the increase of precursor solution. Besides, it seems like the deposition of different organometallic Ag metal precursors has no visible in-fluence on the morphology of WO$_3$ NRs. Further information about the microstructure of the Ag NPs and the WO$_3$ NRs was character-ized by TEM. TEM images of Ag/WO$_3$ sensors with different amounts of Ag-loading produced using the Ag-AMP precursor are shown in Fig. 6. It can be observed that the diameter of WO$_3$ NRs is about 100–200 nm. The clear lattice fringes can be seen in two insets in Fig. 6(b) with interplanar spacings of 0.385 and 0.235 nm, corre-sponding to the (002) plane of WO$_3$ and (111) plane of Ag. The surface of WO$_3$ NRs is homogeneously covered with well-dispersed spherical Ag NPs. The particle size distribution of the Ag NPs with different loadings was counted and the result is shown in Fig. 7. It
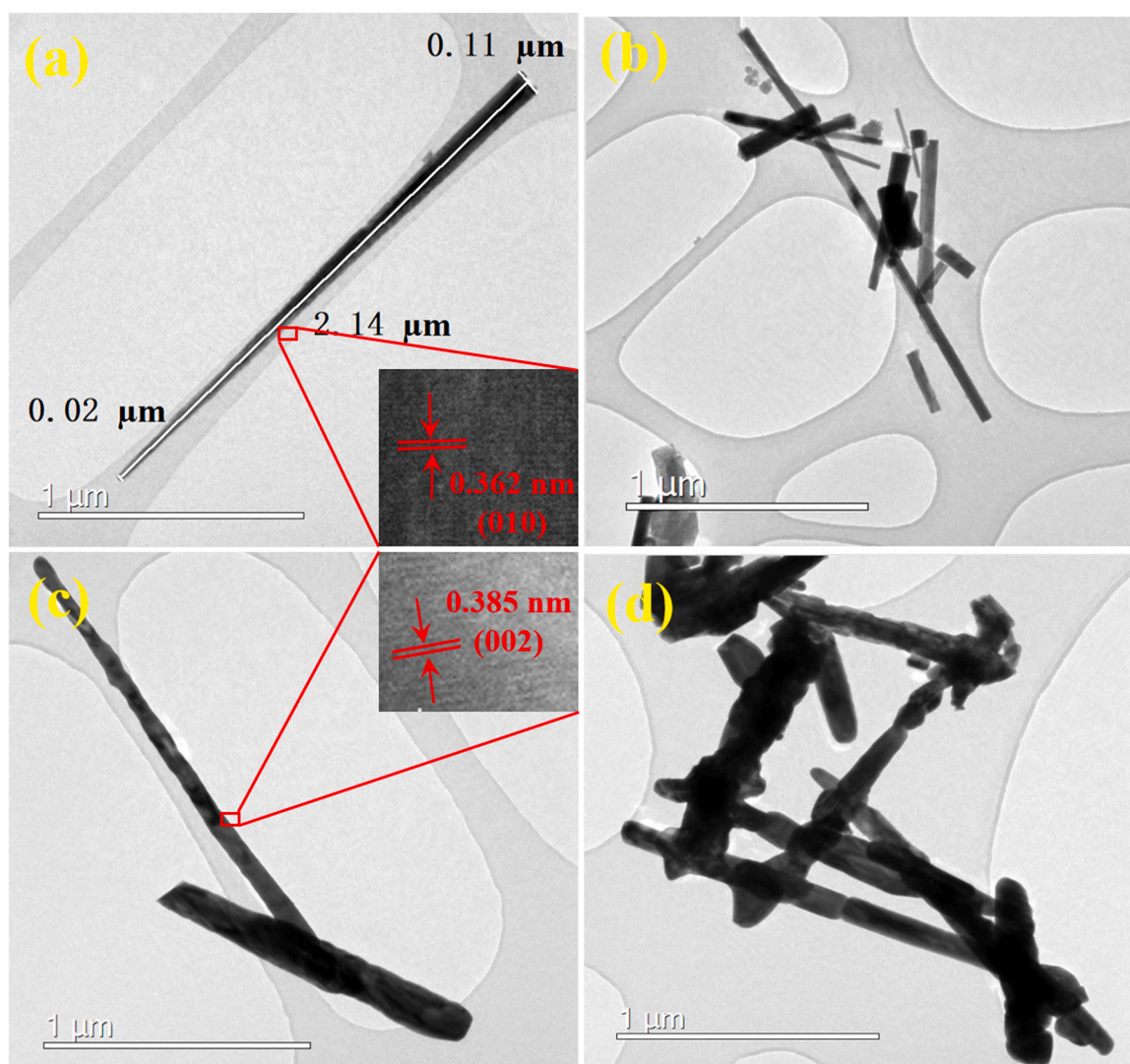
Fig. 4. HRTEM images of (a-b) as-deposited WO_{3-x} NRs and (c-d) annealed WO_3 NRs.

can be found that the diameter of Ag NPs is mostly distributed between 6 and 20 nm irrespective of the precursor amount. EDS element mapping was carried out to study the elemental composition of the as-deposited Ag/WO_3 on the alumina gas sensor platform. From the EDS spectrum of the sample shown in Fig. 8, four main elements, including Au, W, O, and Ag were detected. Particularly, the presence of a large amount of Au elements is derived from the use of a gold TEM grid and the gold electrode from the sensor substrate. Corresponding EDS elemental mapping is shown in Fig. 8(a-d), illustrating that W, O, and Ag are all well distributed along the Ag NPs decorated WO_3 NRs.

The elemental electronic state and the composition of as-deposited WO_{3-x}, annealed WO_3 thin films, and Ag NPs were conducted through XPS analysis. Fig. 9 displays the W 4f and O 1s core-level spectra recorded from the as-deposited WO_{3-x} and WO_3 AA films on alumina sensor platform. As is shown in Fig. 9(a), two doublets of W 4f are obtained after fitting the spectra for as-deposited WO_{3-x}. The peaks at 35.7 and 37.8 eV are associated with W $4f_{7/2}$ and W $4f_{5/2}$ for the W^{6+} oxidation state respectively, referring to

the existence of stoichiometric WO_3. The low-intensity ones at 34.7 and 36.9 eV demonstrate the presence of the sub-stoichiometric WO_{3-x}. After annealing, the W 4f spectra on the sensor shown in Fig. 9(b) reveal only two intense peaks at 35.4 and 37.5 eV, corresponding to W $4f_{7/2}$ and W $4f_{5/2}$ for the W^{6+} oxidation state [27]. The results prove the presence of only stoichiometric WO_3. As displayed in Fig. 9(c,d), the peak located at 530.7 and 530.3 eV can be attributed to the lattice oxygen in the as-deposited WO_{3-x} and WO_3 AA on alumina. Fig. 10 displays the XPS spectra of the Ag3d regions for all three organometallic Ag metal precursors with different volumes of initial precursor solution and their corresponding area ratio of Ag3d to W4f regions. For all samples, two clear peaks at around 374.2 and 368.1 eV are identified clearly and can be assigned to Ag$3d_{3/2}$ and Ag$3d_{5/2}$ respectively. Some small chemical shift for the Ag core level has been observed with different amounts of loadings, which can be attributed to the initial state effect caused by the size of the Ag NPs [28]. For Ag NPs, a 0.5–2 eV chemical shift has been observed for small particles as compared to the core levels of respective bulk Ag crystals [29]. It can be found that the intensity of the Ag peaks for all
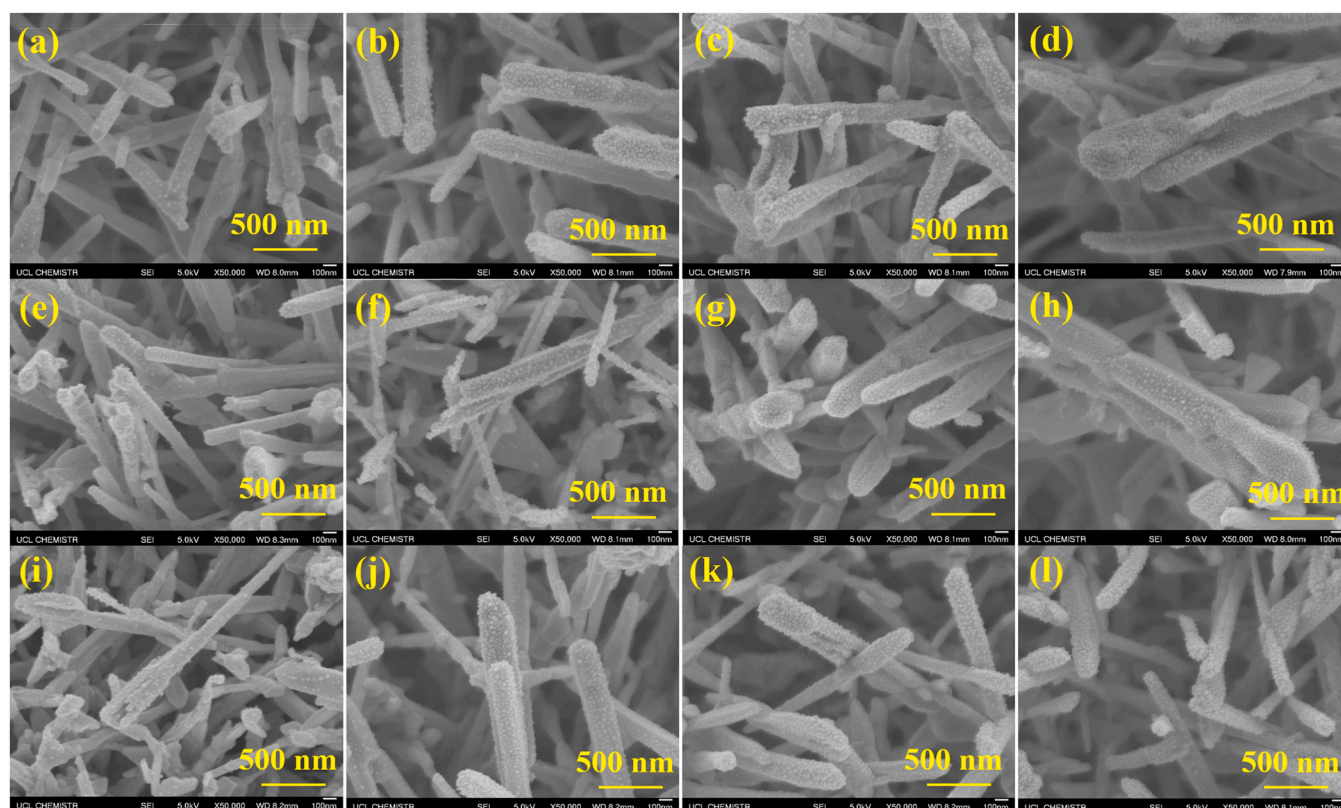
Fig. 5. SEM images of as-deposited Ag/WO₃ sensors by using (a-d) Ag-AMP, (e-h) Ag-AP and (i-l) Ag-EA as precursors with various amounts of the initial precursor solution. (a, e, i) 1 μL, (b, f, j) 3 μL, (c, g, k) 5 μL and (d, h, l) 10 μL.

three organometallic Ag metal precursors increases as the amount of precursor increases. Fig. 10(d-f) show an increase in silver deposition on WO₃ as the amount of Ag precursor solution increase. This would be an important improvement over our previous use of AgNO₃ as a silver precursor, where it was very difficult to alter the amount of Ag/Ag₂O deposited even by changing the amount of precursor. However, it is also worth noting that the increase of area ratio of Ag3d to W4f regions becomes smaller with the further increase of Ag precursor amount.

3.2. Gas sensing properties

Gas sensing tests were carried out to different oxygen concentrations ranging from 0% to 20% (200,00 ppm) in an ambient environment (~50% RH) for all undecorated and Ag-decorated WO₃ sensors at operating temperatures varying from 150 to 300 °C. The relative humidity (RH) was maintained at 50% and the temperature interval was set at 25 °C to examine the sensors' sensing properties. Dynamic response-recovery curves of all Ag-AMP/WO₃, Ag-EA/WO₃, Ag-AP/WO₃, and undecorated WO₃ sensors towards various O₂ concentrations (1–5–10–15–20%) are shown in Fig. 11. It should be pointed out that the sensors of AgAMP 5 μL, AgAMP 1 μL, AgAP 3 μL, and AgEA 1 μL did not successfully pass the sensing tests due to sensor failure to measure resistance through the sensor, heater or both. Obviously, the resistance of all sensors increased upon exposure to O₂ that reduced when subsequently exposed to N₂, revealing a typical n-type semiconductor behavior. In general, the absolute change in resistance on exposure to O₂ of the sensors

decorated using organometallic silver increases with the increasing amount of silver precursors. For the sensors decorated by Ag-AMP and Ag-EA, the amount of 3 μL shows the largest resistance change, while the largest resistance change is observed for 10 μL decorated by Ag-AP. Moreover, the absolute resistance simultaneously increases with the increase of O₂ concentration under the specific temperature, indicating the improvement of sensor response.

Fig. 11(b) shows the response of Ag-AMP 3 μL/WO₃ and WO₃-based sensors at different operating temperatures under the O₂ concentration of 20%. Both sensors exhibit an improvement in the sensor response with the increase of working temperature from 150° to 250 °C. For all the WO₃ sensors, the highest sensing response is obtained at 250 or 300 °C with a value of about 4, while for the Ag-AMP 3 μL/WO₃ sensor, the highest response of 4.4 is found at 300 °C. For the 10 μL Ag-AP decorated WO₃ sensor, the maximum response value of 5 is found at around 240 °C (Fig. 11(d)). It is worth noting that the response decreases sharply in the temperature interval of 250–275 °C and then increases again with the further increase in working temperature, which may be attributed to the change of Ag NPs size under high temperatures and thus affects the sensing performance of the Ag/WO₃ sensors. Besides, for the Ag-EA 3 μL/WO₃ sensor, two max response peaks were found with the response value of 4.4 and 4.7 at 200 and 250 °C, respectively (Fig. 11(f)). The small response peak located at 200 °C could be attributed to the phase change of Ag NPs in bulk with larger particles, and the higher peak positioned at 250 °C refers to the sensing response for Ag NPs with smaller size. Ag forms Ag₂O upon exposure to O₂ over the surface but the obtained Ag₂O tends to decompose and form Ag and O₂
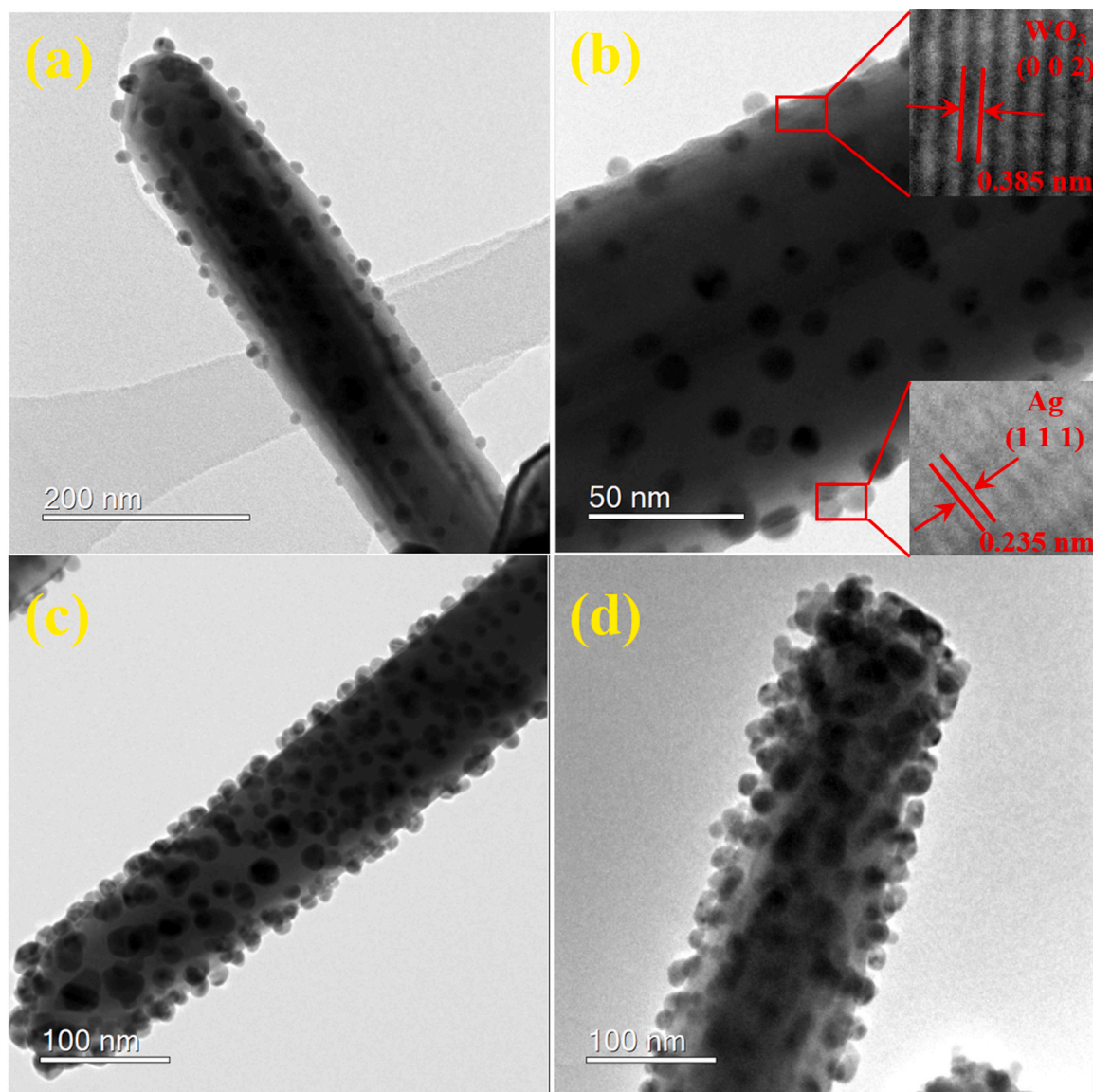
Fig. 6. TEM images of as-deposited Ag/WO₃ sensor by using Ag-AMP as a precursor with various amounts of initial precursor solution (a) 1 μL, (b) 3 μL, (c) 5 μL, and (d) 10 μL.

when the temperature is over 190 °C [30]. Hence at lower temperatures, the silver should be oxidized to Ag_2O, while at high temperatures, it should be decomposed to metallic Ag. However, Barsan et al. [31] concluded that the surface energy of Ag nanostructure may enable Ag_2O to be stable at temperatures from 190 to 700 °C in the air for small-size Ag NPs. Moreover, another published paper reports that Ag was oxidized into Ag_2O at an oxidation temperature of about 350–500 °C [32]. The O_2 response of Ag NPs decorated WO₃ sensors may therefore be directly related to the size, phase, and proportion of Ag/Ag_2O NPs [33–35], and the working temperature is the critical factor to influence these variables. Hence such temperature-induced phenomena might be the cause of the difference between the Ag-AMP 3 μL/WO₃ sensor in Fig. 11(b) where the sensitivity continues to increase with increasing working temperature for whereas fluctuations in response are observed for Ag-AP 10 μL/WO₃ and Ag-EA 3 μL/WO₃ in Fig. 11(d) and 11(f).

3.3. Growth mechanism of the Ag decorated WO₃ NRs

As is well known, two main concepts are often used for the preparation of MOSs, namely 'top-down' fabrication and 'bottom-up' synthesis [36]. Especially, AACVD is considered as the typical 'bottom-up' approach to generating large-scale nanomaterials, which is based on the growth of structures through the assembly of atoms derived from chemical precursors. The basis of AACVD is the atomization of liquid precursor which is transported by a flow of inert carrier gas to the substrate. The solvent then undergoes rapid vaporation, forming precursor vapors at elevated temperatures, the vapors start to react and decompose forming a thin film on the substrate. Film morphology such as nanostructured rods is dependent on the solvent used and the deposition temperature.

It is widely accepted that the formation of WO₃ NRs follows the catalyst-free direct vapor-solid (VS) mechanism [37]. Fig. 12 shows
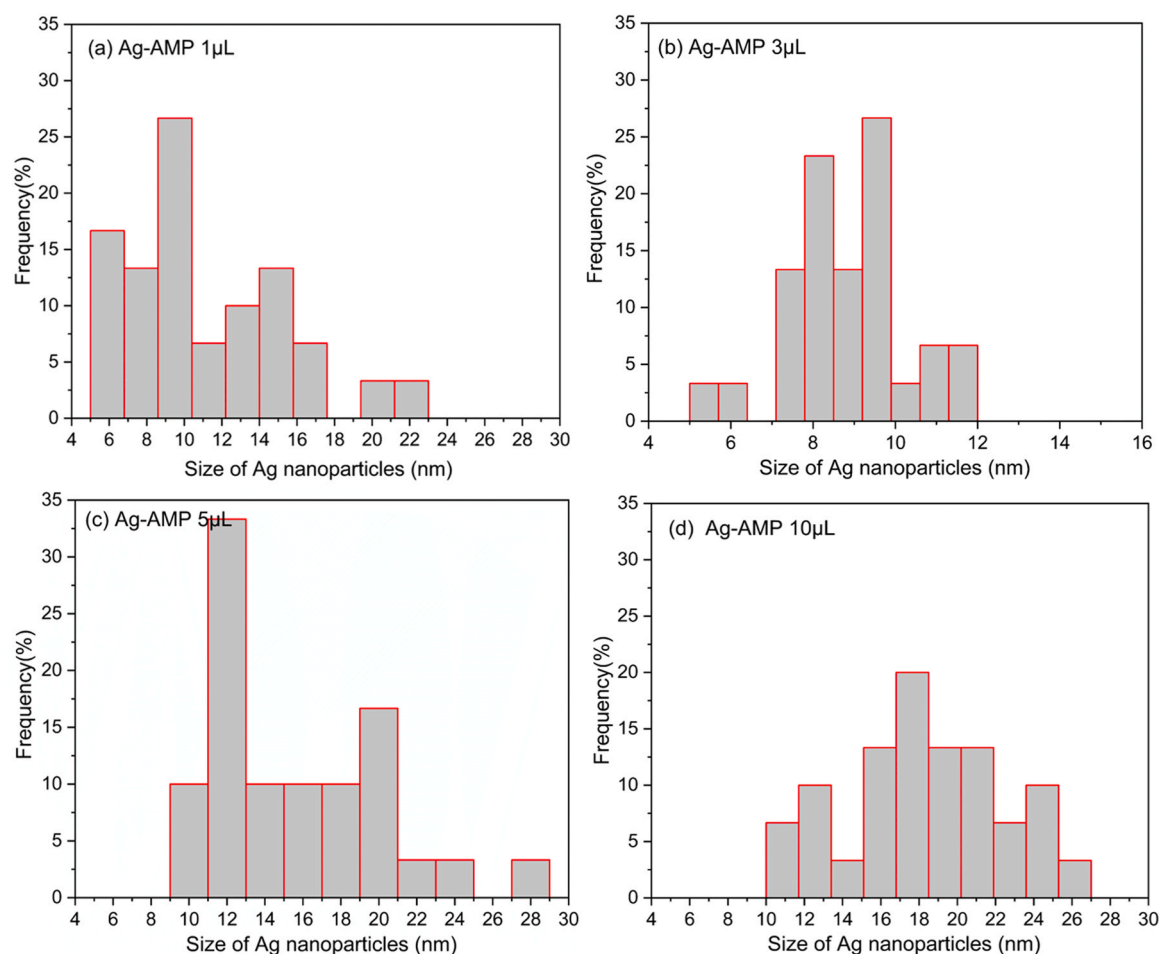
Fig. 7. Size distribution of Ag nanoparticles on WO$_3$ sensors using Ag-AMP precursors (a) 1 μL, (b) 3 μL, (c) 5 μL and (d) 10 μL.

the growth mechanism for Ag-decorated WO$_3$ NRs. First of all, vapor phase WO$_3$ is obtained via the direct oxidation of the tungsten organic precursor. The generated WO$_3$ vapor is carried by the N$_2$, followed by the formation of localized crystals at the incipient stages. Then, the WO$_3$ polycrystalline layer tends to form on the surface of alumina sensing substrate, and the polycrystalline layer in the morphology of thin films consists of NPs, which can serve as seeds and is vital for the nucleation and subsequent growth of WO$_3$ NRs [38]. The nanostructured film can offer energetically favorable planes for the nucleation of the NRs end caps. Furthermore, it can provide pathways for surface diffusion of subsequently condensed vapor species to the surface of WO$_3$ NRs. The loosely packed [010] crystallographic planes are considered as the preferred grow surface owing to the relatively high surface energy and fast growth rate. As a result, the nanorods with single crystals lift and exhibit a high length-to-diameter ratio. Especially, the growth of WO$_3$ NRs is crossed like a lawn due to the rough surface of the initial polycrystalline layer. Based on the observation of the cross-section in Fig. 3(b), the lawn-structured WO$_3$ thin film is generated. Besides, it should be clear that some factors such as the degree of supersaturation, the transfer rate of WO$_3$ vapor, availability of nucleation

sites, and temperature gradient across the substrate are crucial during the nucleation and growth of WO$_3$ NRs.

After the successful synthesis of WO$_3$ NRs, organometallic silver precursors were used to deposit Ag NPs on the surface of WO$_3$ NRs. WO$_3$ NRs with a high length-to-diameter ratio have high surface energy, which can act as active attachment sites to attract organometallic silver vapor molecules. Since the heating temperature in the AACVD reactor is relatively high, the Ag-containing precursors will decompose and generate Ag NPs. Besides, the WO$_3$ NRs are fully exposed to the environment of organometallic silver vapor, and thus the decoration of Ag NPs is well-dispersed. With the volume increase of the Ag precursor solutions, the loading of Ag NPs becomes densely packed.

3.4. Gas sensing mechanism

For most of the chemiresistive metal oxide gas sensors, a band bending model based on the surface chemistry of highly reactive ionosorbed species (O$_2^-$, O$^-$ or O^{2-}) was usually put forwards to illustrate the gas sensing mechanism [39]. However, it has been proved that the classical band bending model is inappropriate for
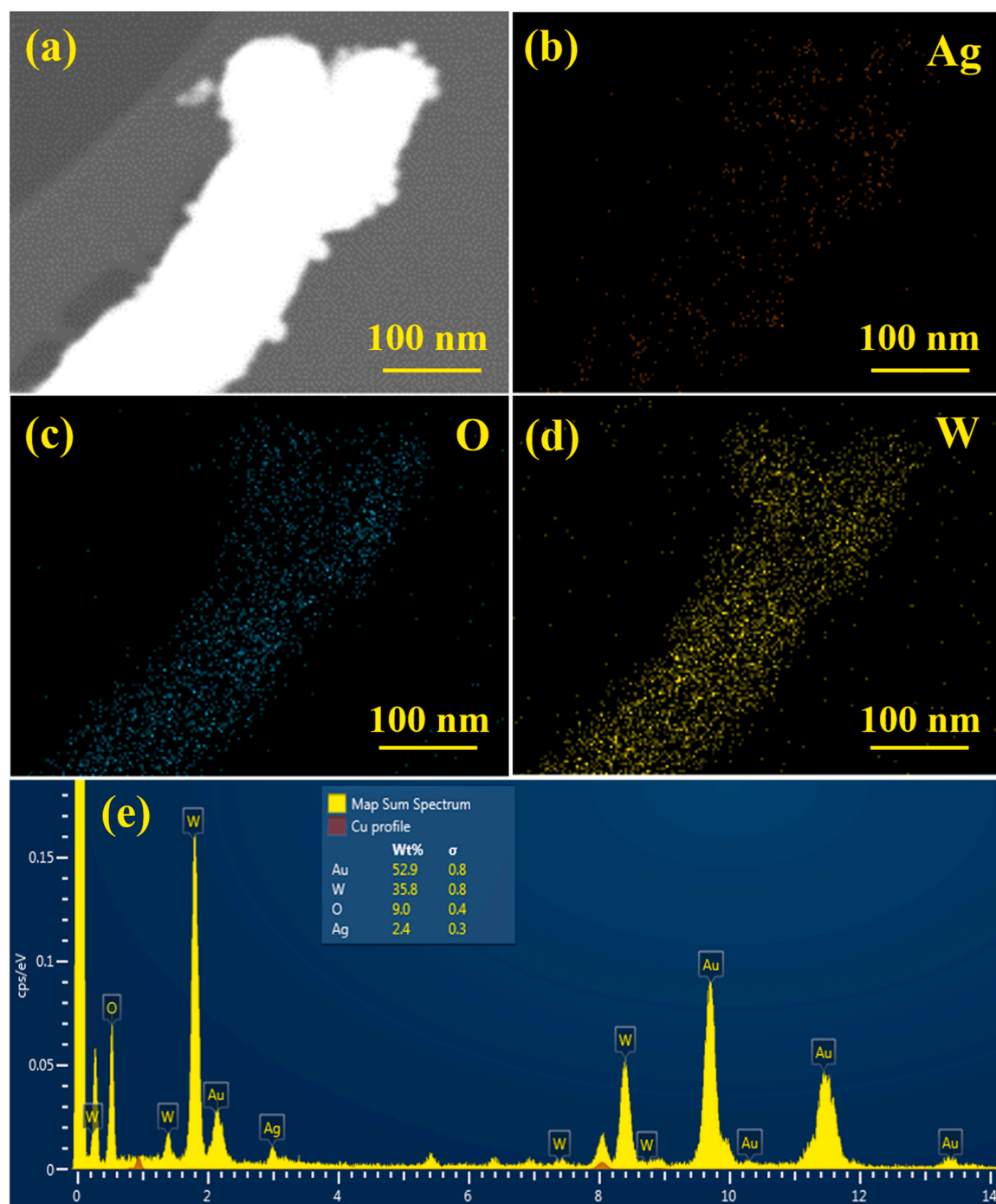
Fig. 8. EDS mapping images of Ag/WO$_3$ on sensor platform (a) electronic image of Ag/WO$_3$ sample, (b) Ag distribution, (c) O distribution, (d) W distribution and (e) EDS spectrum of the Ag/WO$_3$ sensor sample.

WO$_3$-based sensors, in which surface lattice oxygen instead of surface adsorbed charged oxygen species reacts with the adsorbed target gases to create oxygen vacancies that rapidly diffuse into the bulk and modulate the conductivity [40]. Frederick et al. [41] developed a "bulk conduction mechanism" to explain the gas sensing behavior that the resistance change of the gas sensors should be attributed to the change of oxygen vacancy concentration in the nanomaterial. In the framework of this bulk conduction mechanism,

in the starting N$_2$ ambient, there is a higher concentration of oxygen vacancies on the surface of Ag/WO$_3$ sensors and hence higher conductivity, then after the sensor is exposed to O$_2$, there will be a lower concentration of oxygen vacancies due to vacancy healing (Fig. 13(a)).

The role of catalyst particles in sensitizing MOSs has been discussed in the context of two mechanisms, namely chemical and electronic sensitization [42]. By adding Ag NPs to the surface of
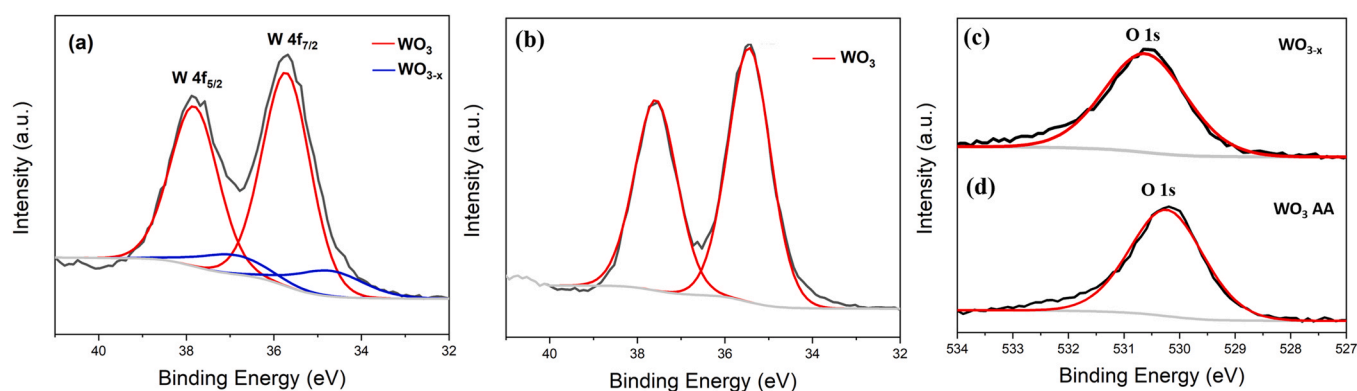
Fig. 9. XPS W 4 f core-level spectra of (a) as-deposited WO$_{3-x}$ and (b) WO$_3$ AA on alumina sensor, XPS O 1 s core-level spectra of (a) as-deposited WO$_{3-x}$ and (b) WO$_3$ AA on alumina sensor.
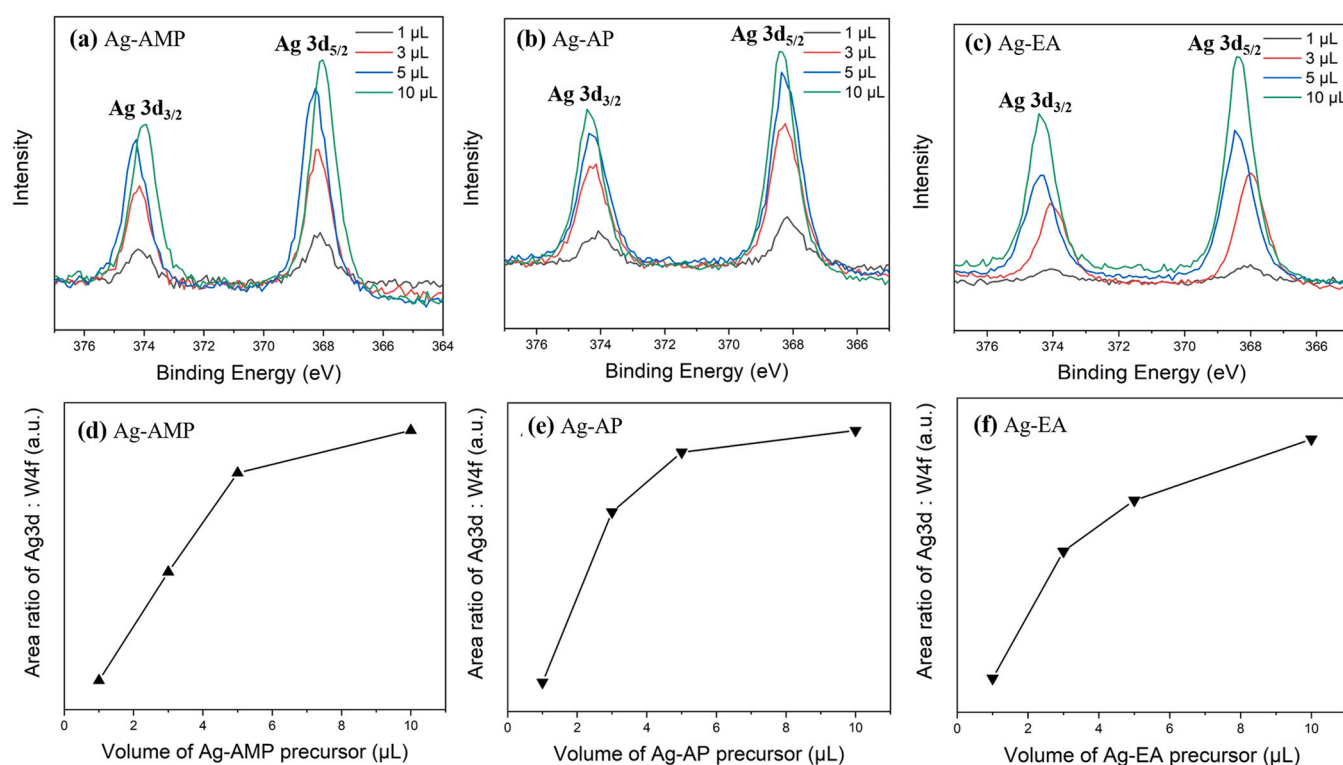

Fig. 10. XPS Ag3d core-level spectra of (a)Ag-AMP, (b) Ag-AP, and (c) Ag-EA with various volumes of initial precursor solution used and their corresponding area ratio Ag 3d: W 4f (d) Ag-AMP, (e) Ag-AP and (f) Ag-EA.

WO$_3$, the possible contribution in sensitivity to oxygen can be ascribed to the function of electronic sensitization derived from the interface between Ag NPs and the WO$_3$ surface and the effect of chemical sensitization of Ag NPs (spill-over effect). The data found in the literature showed a relatively low work function of Ag (4.26 eV) [43] and a high work function of WO$_3$ (5.7 eV) [44], resulting in electrons transferring from Ag NPs to n-type semiconductor WO$_3$ (electronic sensitization) in order to equalize the Fermi level, as shown in Fig. 13(b), which would lead to a decrease in baseline resistance. Conversely, more oxygen molecules can be adsorbed by the Ag/WO$_3$ surface through a spill-over type mechanism under chemical sensitization, reducing the oxygen vacancy concentration, which will increase the baseline resistance. The net dramatic increase in the baseline resistance indicates that the spill-over effect is more dominant (increases baseline resistance) here than electronic sensitization (decreases baseline resistance). Hence the introduction of Ag NPs will enrich the surface with lattice oxygen, which will lead to the decline of vacancy concentration and the increase of initial resistance of Ag/WO$_3$ sensors [45].
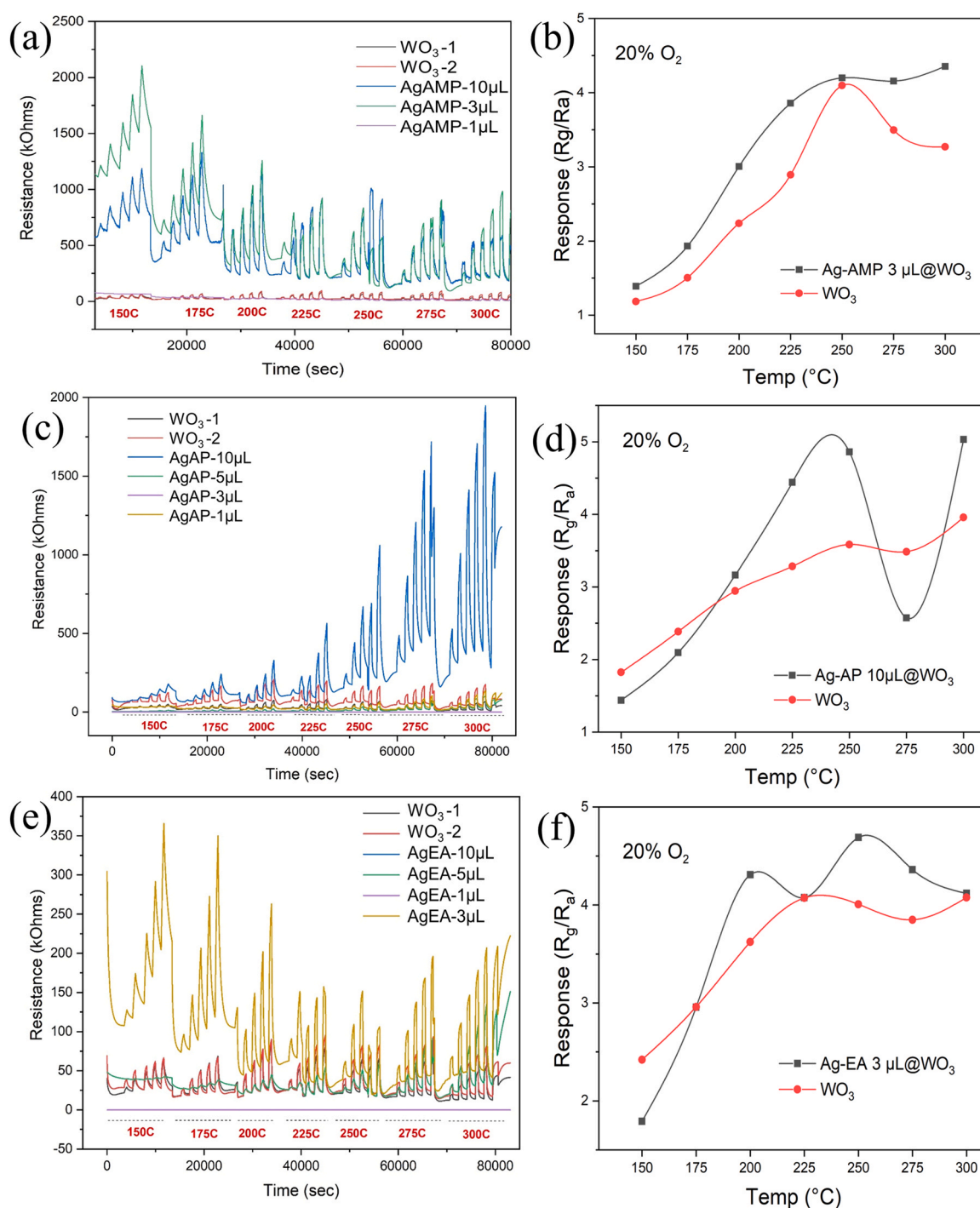
Fig. 11. Sensor resistance changes of (a) Ag-AMP/WO$_3$ sensors, (c) Ag-AP/WO$_3$ sensors, and (e) Ag-EA/WO$_3$ sensors to various O$_2$ concentrations (1–5–10–15–20%) at different operating temperatures ranging from 150° to 300°C with an undecorated WO$_3$ for comparison; (b) response of WO$_3$ and Ag-AMP 3 µL/WO$_3$ sensor to 20% O$_2$ as a function of operating temperatures; (d) response of WO$_3$ and Ag-AP 10 µL/WO$_3$ sensor to 20% O$_2$ as a function of operating temperatures; (f) response of WO$_3$ and Ag-EA 3 µL/WO$_3$ sensor to 20% O$_2$ as a function of operating temperatures.
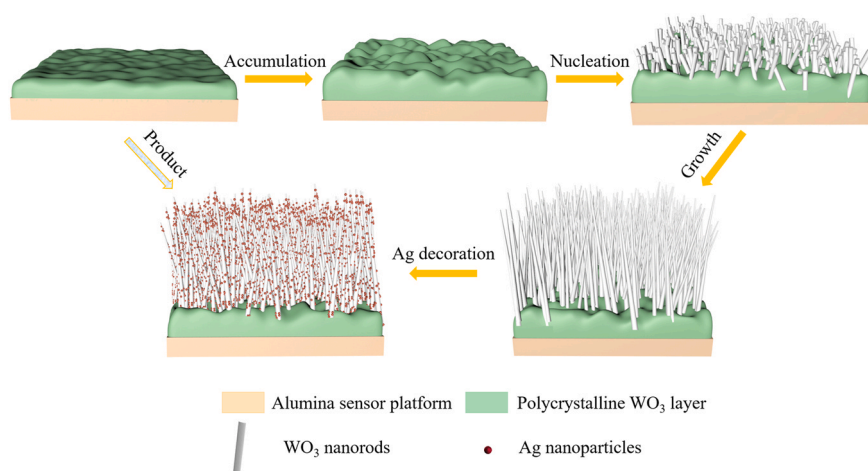
Fig. 12. Schematic model of the growth mechanism for Ag-decorated WO$_3$ NRs.
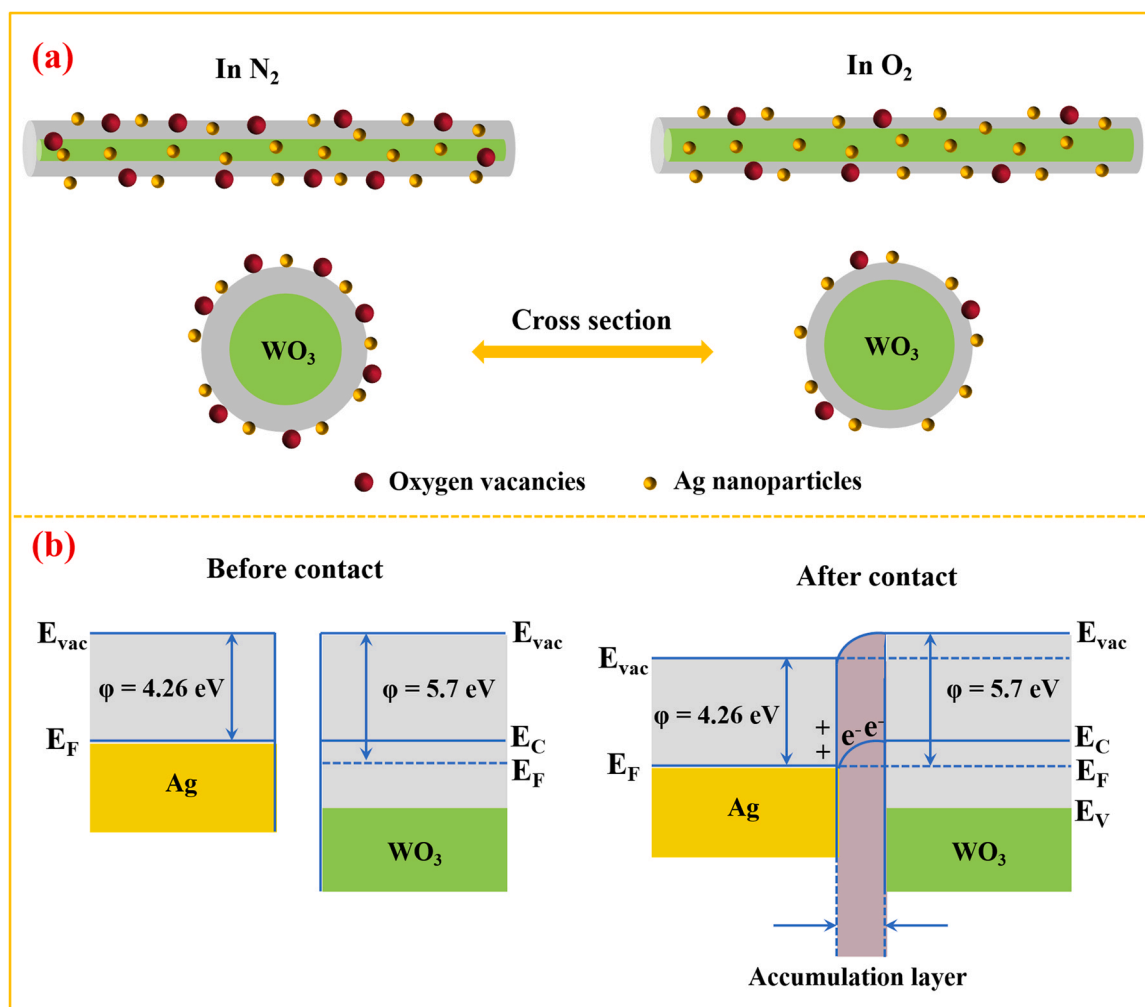

Fig. 13. (a) Energy band structure schematic diagrams of Ag and n-type WO$_3$ semiconductors. (b) Schematic model of depletion layer for undecorated WO$_3$ NRs and Ag decorated WO$_3$ NRs when exposed to N$_2$ and O$_2$.

4. Conclusions

Ag NPs-decorated WO_3 NRs using organometallic silver as the precursor was successfully deposited on the alumina sensor platform in a two-step synthesis method via AACVD. The physical property characterization results showed that no obvious Ag peaks were found in the XRD patterns of a Ag-decorated WO_3 gas sensor due to the overlap of Au peaks. XPS analysis demonstrated that metallic Ag NPs were formed on the surface of WO_3 NRs. Together with the SEM images, it can be observed that the coverage of spherical Ag NPs adhered on the surface of WO_3 NRs increased with the increase of precursor amount and tend to approach saturation when the dosage reaches 10 μL. The diameter of the Ag NPs is mainly ranging from 9 to 13 nm while the diameter of WO_3 NRs is about 100–200 nm and the length is varying from 600 nm to several μm. Although gas sensing measurements indicated that no significant enhancement was found for the Ag-decorated WO_3 NRs in the O_2 sensing response as compared to the bare WO_3 NRs, the preparation process of Ag NPs-decorated WO_3 NRs is very informative because the silver loading can be controlled simply by altering the silver precursor amount. Further development and investigation on sensor selectivity, stability, and cross-sensitivity to other gases need to be studied in the future to make Ag-decorated WO_3-based materials a potential oxygen gas sensor.

CRediT authorship contribution statement

Yiyun Zhu completed experimental design, materials characterization, data analysis and wrote the paper for submission. Chris Blackman provided critical comments on this paper. Sai Kiran Ayyala and James A. Covington contributed to the gas sensing measurements and design of the sensor devices. Pengfei Zhou edited the written work of YZ and dealt with the editorial process. Yanbai Shen and Jinsheng Liang contributed to the description of the sensing mechanism. Caroline Knapp and Ye Zhou provided the organometallic silver precursors. Xiangxi Zhong contributed to discussions on the gas sensing context of the research reported.

Data availability

Data will be made available on request.

Declaration of Competing Interest

The authors declare that they have no known competing financial interests or personal relationships that could have appeared to influence the work reported in this paper.

Acknowledgments

References

[1] Y. Wang, X. Lai, B. Liu, Y. Chen, Y. Lu, F. Wang, L. Zhang, UV-induced desorption of oxygen at the TiO_2 surface for highly sensitive room temperature O_2 sensing, J. Alloy. Compd. 793 (2019) 583–589.

[2] X. Yang, Y. Li, Construction and O_2 sensing performance of a core–shell structured magnetic-mesoporous composite functionalized with a ruthenium complex, Microporous Mesoporous Mater. 215 (2015) 84–90.

[3] W.P. Sari, C. Blackman, Y. Zhu, J.A. Covington, AACVD grown WO_3 nanorods decorated with Ag/Ag_2O nanoparticles for oxygen measurement in a humid environment, IEEE Sens. J. 19 (2019) 826–832.

[4] T. Stoycheva, F.E. Annanouch, I. Gràcia, E. Llobet, C. Blackman, X. Correig, S. Vallejos, Micromachined gas sensors based on tungsten oxide nanorods directly integrated via aerosol assisted CVD, Sens. Actuators B 198 (2014) 210–218.

[5] R.L. Wilson, C.E. Simion, A. Stanoiu, A. Taylor, S. Guldin, J.A. Covington, C.J. Carmalt, C.S. Blackman, Humidity-tolerant ultrathin NiO gas-sensing films, ACS Sens. 5 (2020) 1389–1397.

[6] C.-M. Wu, S. Naseem, M.-H. Chou, J.-H. Wang, Y.-Q. Jian, Recent advances in tungsten-oxide-based materials and their applications, Front. Mater. 6 (2019).

[7] C. Dong, R. Zhao, L. Yao, Y. Ran, X. Zhang, Y. Wang, A review on WO_3 based gas sensors: morphology control and enhanced sensing properties, J. Alloy. Compd. 820 (2020) 153194.

[8] P. Jaroenapibal, P. Boonma, N. Saksilaporn, M. Horprathum, V. Amornkitbamrung, N. Triroj, Improved NO_2 sensing performance of electrospun WO_3 nanofibers with silver doping, Sens. Actuators B 255 (2018) 1831–1840.

[9] Y. Wang, J. Liu, X. Cui, Y. Gao, J. Ma, Y. Sun, P. Sun, F. Liu, X. Liang, T. Zhang, G. Lu, NH_3 gas sensing performance enhanced by Pt-loaded on mesoporous WO_3, Sens. Actuators B 238 (2017) 473–481.

[10] F.E. Annanouch, Z. Haddi, S. Vallejos, P. Umek, P. Guttmann, C. Bittencourt, E. Llobet, Aerosol-assisted CVD-grown WO_3 nanorods decorated with copper oxide nanoparticles for the selective and humidity-resilient detection of H_2S, ACS Appl. Mater. Interfaces 7 (2015) 6842–6851.

[11] F. Annanouch, S. Vallejos, C. Blackman, X. Correig, E. Llobet, CO and H_2 sensing with CVD-grown tungsten oxide nanorods decorated with Au, Pt or Cu nanoparticles, Procedia Eng. 47 (2012) 904–907.

[12] A. Cisquella-Serra, M. Magnani, M. Madou, M. Gamero-Castaño, Conformal CVD of WO_{3-x} on electrospun carbon nanofiber mats assisted by Joule heating, Carbon 195 (2022) 27–34.

[13] S. Wang, M. Li, L. Ren, Y. Wu, L. Li, Sensing performance for ethylene glycol of hydrothermally self-assembled 3D WO_3, Ceram. Int. (2022).

[14] R. Senthilkumar, G. Ravi, C. Sekar, M. Arivanandhan, M. Navaneethan, Y. Hayakawa, Determination of gas sensing properties of thermally evaporated WO_3 nanostructures, J. Mater. Sci. Mater. Electron 26 (2015) 1389–1394.

[15] C.-P. Li, F. Lin, R.M. Richards, C. Engtrakul, A.C. Dillon, R.C. Tenent, C.A. Wolden, Ultrasonic spray deposition of high performance WO_3 films using template-assisted sol–gel chemistry, Electrochem. Commun. 25 (2012) 62–65.

[16] F.E. Annanouch, S. Vallejos, T. Stoycheva, C. Blackman, E. Llobet, Aerosol assisted chemical vapour deposition of gas-sensitive nanomaterials, Thin Solid Films 548 (2013) 703–709.

[17] C.S. Blackman, X. Correig, V. Katko, A. Mozalev, I.P. Parkin, R. Alcubilla, T. Trifonov, Templated growth of tungsten oxide micro/nanostructures using aerosol assisted chemical vapour deposition, Mater. Lett. 62 (2008) 4582–4584.

[18] S. Vallejos, P. Umek, C. Blackman, Aerosol assisted chemical vapour deposition control parameters for selective deposition of tungsten oxide nanostructures, J. Nanosci. Nanotechnol. 11 (2011) 8214–8220.

[19] X. Yang, Y. Wang, H. Fu, W. Wang, D. Han, X. An, Experimental and theoretical study on the excellent amine-sensing performance of Au decorated WO_3 needle-like nanocomposites, Mater. Chem. Phys. 234 (2019) 122–132.

[20] C. Navío, S. Vallejos, T. Stoycheva, E. Llobet, X. Correig, R. Snyders, C. Blackman, P. Umek, X. Ke, G. Van Tendeloo, C. Bittencourt, Gold clusters on WO_3 nanorods grown via AACVD: XPS and TEM studies, Mater. Chem. Phys. 134 (2012) 809–813.

[21] S. Vallejos, T. Stoycheva, P. Umek, C. Navio, R. Snyders, C. Bittencourt, E. Llobet, C. Blackman, S. Moniz, X. Correig, Au nanoparticle-functionalised WO_3 nanorods and their application in high sensitivity gas sensor devices, Chem. Commun. 47 (2011) 565–567.

[22] S. Vallejos, P. Umek, T. Stoycheva, F. Annanouch, E. Llobet, X. Correig, P. De Marco, C. Bittencourt, C. Blackman, Single-step deposition of Au- and Pt-nanoparticle-functionalized tungsten oxide nanorods synthesized via aerosol-assisted CVD, and used for fabrication of selective gas microsensor arrays, Adv. Funct. Mater. 23 (2013) 1313–1322.

[23] H.R. Tinker, M.A. Bhide, E. Magliocca, T.S. Miller, C.E. Knapp, Synthetic tethered silver nanoparticles on reduced graphene oxide for alkaline oxygen reduction catalysis, J. Mater. Sci. 56 (2021) 6966–6976.

[24] S. Vallejos, I. Gràcia, E. Figueras, C. Cané, Nanoscale heterostructures based on Fe_2O_3@WO_{3-x} nanorods and their direct integration into flexible transducing platforms for toluene sensing, ACS Appl. Mater. Interfaces 7 (2015) 18638–18649.

[25] W. Geng, Z. Ma, Y. Zhao, X. He, L. Duan, J. Tu, Q. Zhang, The self-assembly of octahedral Cu_xO and its triethylamine-sensing properties, Sens. Actuators B 312 (2020) 128014.

[26] M. Ling, C.S. Blackman, R.G. Palgrave, C. Sotelo-Vazquez, A. Kafizas, I.P. Parkin, Nanorod arrays: correlation of optical properties, electronic structure, and photocatalytic activity in nanostructured tungsten oxide, Adv. Mater. Interfaces 4 (2017).

[27] È. Navarrete, C. Bittencourt, X. Noirfalise, P. Umek, E. González, F. Güell, E. Llobet, WO_3 nanowires loaded with cobalt oxide nanoparticles, deposited by a two-step AACVD for gas sensing applications, Sens. Actuators B 298 (2019) 126868.

[28] B. Richter, H. Kuhlenbeck, H.J. Freund, P.S. Bagus, Cluster core-level binding-energy shifts: the role of lattice strain, Phys. Rev. Lett. 93 (2004) 026805.

[29] I. Lopez-Salido, C.L. Dong, Y.D. Kim, Ag nanoparticles on highly ordered pyrolytic graphite (HOPG) surfaces studied using STM and XPS, Surf. Sci. 588 (2005) 6–18.

[30] S.-W. Choi, A. Katoch, G.-J. Sun, P. Wu, S.S. Kim, NO_2-sensing performance of SnO_2 microrods by functionalization of Ag nanoparticles, J. Mater. Chem. C 1 (2013) 2834–2841.

[31] N. Barsan, M. Schweizer-Berberich, W. Göpel, Fundamental and practical aspects in the design of nanoscaled SnO$_2$ gas sensors: a status report, Fresenius' J. Anal. Chem. 365 (365) (1999) 287–304.

[32] T.T. Ngoc Hoa, N. Van Duy, C.M. Hung, N. Van Hieu, H.H. Hau, N.D. Hoa, Dip-coating decoration of Ag$_2$O nanoparticles on SnO$_2$ nanowires for high-performance H$_2$S gas sensors, RSC Adv. 10 (2020) 17713–17723.

[33] H. Yu, J. Li, Y. Tian, Z. Li, Environmentally friendly recycling of SnO$_2$/Sn$_3$O$_4$ from tin anode slime for application in formaldehyde sensing material by Ag/Ag$_2$O modification, J. Alloy. Compd. 765 (2018) 624–634.

[34] H. Li, Y. He, P. Jin, Y. Cao, M. Fan, X. Zou, G. Li, Highly selective detection of trace hydrogen against CO and CH$_4$ by Ag/Ag$_2$O–SnO$_2$ composite microstructures, Sens. Actuators B 228 (2016) 515–522.

[35] I.-S. Hwang, J.-K. Choi, H.-S. Woo, S.-J. Kim, S.-Y. Jung, T.-Y. Seong, I.-D. Kim, J.-H. Lee, Facile control of C$_2$H$_5$OH sensing characteristics by decorating discrete Ag nanoclusters on SnO$_2$ nanowire networks, ACS Appl. Mater. Interfaces 3 (2011) 3140–3145.

[36] N. Abid, A.M. Khan, S. Shujait, K. Chaudhary, M. Ikram, M. Imran, J. Haider, M. Khan, Q. Khan, M. Maqbool, Synthesis of nanomaterials using various top-down and bottom-up approaches, influencing factors, advantages, and disadvantages: a review, Adv. Colloid Interface Sci. 300 (2022) 102597.

[37] M. Ling, C. Blackman, Growth mechanism of planar or nanorod structured tungsten oxide thin films deposited via aerosol assisted chemical vapour deposition (AACVD), Phys. Status Solidi C 12 (2015) 869–877.

[38] S. Vallejos, I. Gràcia, E. Figueras, C. Cané, Catalyst-free vapor-phase method for direct integration of gas sensing nanostructures with polymeric transducing platforms, J. Nanomater. 2014 (2014) 932129.

[39] G. Li, Y. Shen, S. Zhao, J. Bai, S. Gao, W. Liu, D. Wei, D. Meng, X. San, Construction of rGO-SnO$_2$ heterojunction for enhanced hydrogen detection, Appl. Surf. Sci. 585 (2022) 152623.

[40] C. Blackman, Do we need "Ionosorbed" oxygen species? (Or, "A surface conductivity model of gas sensitivity in metal oxides based on variable surface oxygen vacancy concentration"), ACS Sens. 6 (2021) 3509–3516.

[41] A. Reghu, L.J. LeGore, J.F. Vetelino, R.J. Lad, B.G. Frederick, Distinguishing bulk conduction from band bending transduction mechanisms in chemiresistive metal oxide gas sensors, J. Phys. Chem. C 122 (2018) 10607–10620.

[42] X. Chen, S. Zhao, P. Zhou, B. Cui, W. Liu, D. Wei, Y. Shen, Room-temperature NO$_2$ sensing properties and mechanism of CuO nanorods with Au functionalization, Sens. Actuators B 328 (2021) 129070.

[43] Y. Yin, F. Li, N. Zhang, S. Ruan, H. Zhang, Y. Chen, Improved gas sensing properties of silver-functionalized ZnSnO$_3$ hollow nanocubes, Inorg. Chem. Front. 5 (2018) 2123–2131.

[44] Y. Shen, T. Li, X. Zhong, G. Li, A. Li, D. Wei, Y. Zhang, K. Wei, Ppb-level NO$_2$ sensing properties of Au-doped WO$_3$ nanosheets synthesized from a low-grade scheelite concentrate, Vacuum 172 (2020) 109036.

[45] D. Degler, U. Weimar, N. Barsan, Current understanding of the fundamental mechanisms of doped and loaded semiconducting metal-oxide-based gas sensing materials, ACS Sens. 4 (2019) 2228–2249.